Volume 28
Number 10
9 March 2026
Pages 4305-4692

# Green Chemistry

Cutting-edge research for a greener sustainable future

rsc.li/greenchem

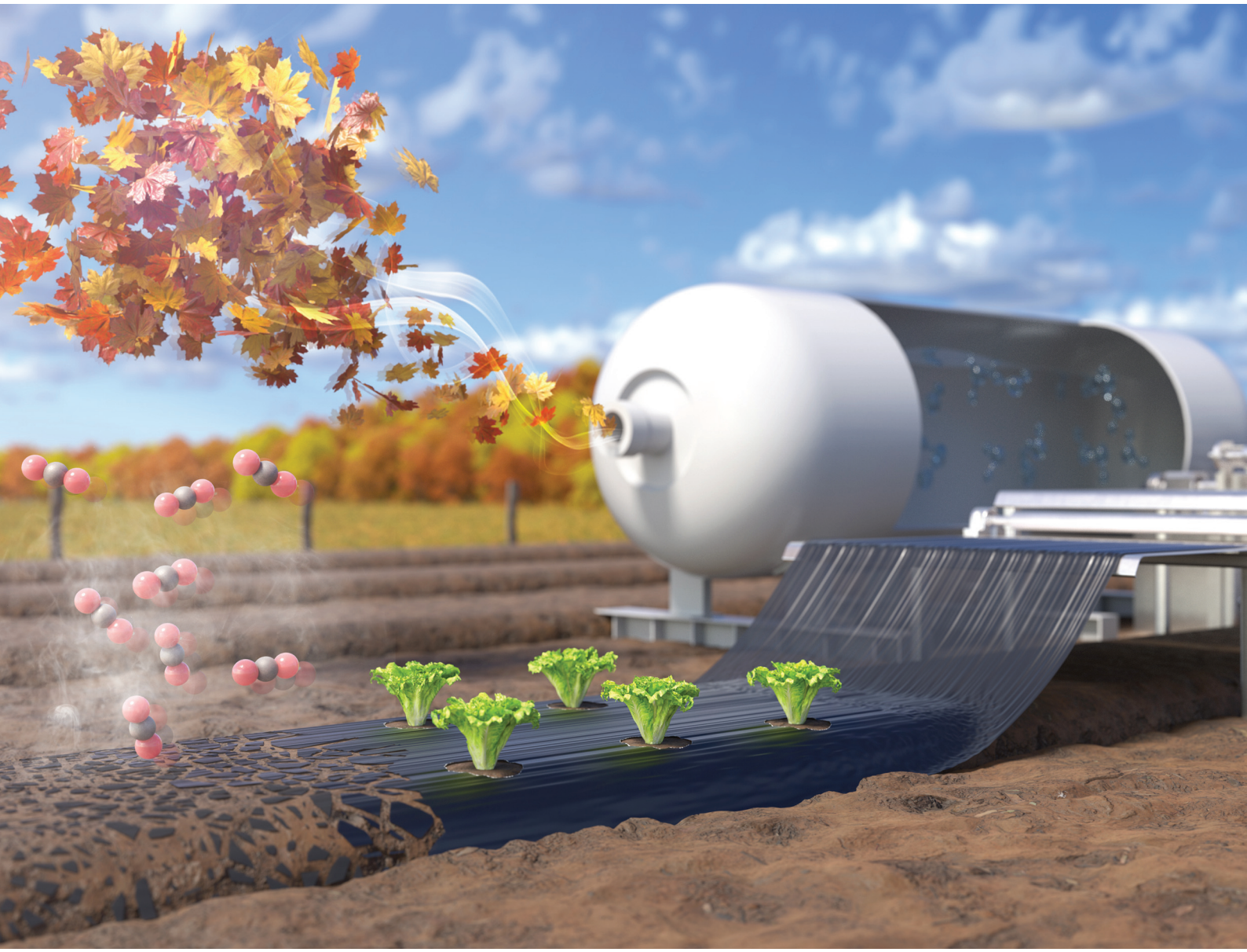

ISSN 1463-9262

ROYAL SOCIETY OF CHEMISTRY

**PAPER**

Jaewook Myung *et al.*

All-water-based fabrication of biodegradable mulch films from dead leaves *via* complex hydrogen-bonded networks

Green Chemistry

PAPER

View Article Online
View Journal | View Issue



Cite this: *Green Chem.*, 2026, **28**, 4449

# All-water-based fabrication of biodegradable mulch films from dead leaves *via* complex hydrogen-bonded networks

Pham Thanh Trung Ninh, [a] Shinhyeong Choe, [a] Yongjun Cho, [a] Hoseong Moon[b] and Jaewook Myung *[a,b]

The escalating accumulation of plastic waste in agricultural soils underscores the urgent need for sustainable alternatives to conventional polyethylene (PE) mulch films. Here, we report the fabrication of high-strength, biodegradable mulch films derived from lignocellulose nanofibers (LCNFs) extracted from a biomass of abundant, non-edible dead leaves. LCNFs were isolated using a hydrated multi-carboxylic acid deep eutectic solvent (DES) coupled with high-intensity ultrasonication. The resulting LCNFs were then blended with cellulose nanocrystals (CNCs), polyvinyl alcohol (PVA), and glycerol (Gly) at varying ratios, using water as the only processing medium to construct lignin-containing all-nanocellulose-combined PVA (LANC/PVA) films through evaporation-induced self-assembly. The incorporation of CNCs and PVA into the LCNF matrix reduced film porosity, yielding denser, smoother, and mechanically stronger structures. Moreover, the high compatibility of LCNFs, CNCs, Gly, and PVA facilitated the formation of an extensive and stable hydrogen bonding network, which contributed to excellent performance characteristics, including improved hydrophobicity (WCA = 77.8–118.6°), low water vapor permeability (WVP = 1.93–5.7 g μm ($m^2$ day Pa)$^{-1}$), complete UV radiation blocking (~100% for both UVA and UVB), and effective soil moisture retention (~5% loss over 14 days). Notably, the soil biodegradation test employing a respirometer revealed that the LANC/PVA films degraded by approximately 34.4 ± 0.9% within 115 days, while ecotoxicity assessments confirmed negligible adverse effects on the germination and growth of monocotyledonous (ryegrass) and dicotyledonous (tatsoi) plants. These findings highlight the potential of dead leaf-derived LANC/PVA films as high-performance, biodegradable mulch films for environmentally responsible plasticulture.

Received 8th December 2025,
Accepted 19th January 2026

DOI: 10.1039/d5gc06616f

rsc.li/greenchem



### Green foundation

1. Our work advances green chemistry by upcycling dead-leaf biomass into biodegradable mulch films through a deep eutectic solvent (DES) pretreatment and water-based processing. This additive- and solvent-minimized approach transforms an abundant waste stream into high-value agricultural materials while enabling a circular lifecycle, as the films safely mineralize in soil after use.
2. The films show strong mechanical, moisture-barrier, and UV-shielding performance and achieve ~35% biodegradation within 115 days under ambient soil conditions. Importantly, post-use soils show no phytotoxic effects, demonstrating a benign end-of-life profile and a viable alternative to persistent polyethylene mulch.
3. Further greening could be achieved by enhancing biodegradation rates, improving DES recovery and recycling, and replacing PVA with fully bio-based, biodegradable matrices. Future work will quantify these gains through a comprehensive lifecycle assessment.

## 1. Introduction

Plastics are indispensable materials in modern society because of their low cost, durability, and versatility.[1] However, their persistence—often spanning centuries—has led to their accumulation across diverse environments,[2] posing a major threat to ecosystems and human health.[3] Despite these concerns, annual global plastic waste continues to rise—projected to reach 1.01 billion tons by 2060—while truly biodegradable plastics represent only a minor fraction.[4,5]

Agriculture represents one of the largest sectors of plastic use, with approximately 12.5 million tons used annually, nearly half in the form of mulch films.[6] These films enhance crop productivity by suppressing weeds, reducing soil moist-

[a]*Department of Civil and Environmental Engineering, Korea Advanced Institute of Science and Technology, Daejeon 34141, Republic of Korea.*
*E-mail: jjaimyung@kaist.ac.kr*
[b]*Graduate School of Green Growth and Sustainability, Korea Advanced Institute of Science and Technology, Daejeon 34141, Republic of Korea*

ure loss, improving nutrient-use efficiency, and promoting earlier harvests through microclimate modification. These benefits contribute to increased production, crop conservation, and reduced agrochemical use.[7] However, the predominance of non-degradable mulch films, such as low- and high-density polyethylene (LDPE, HDPE), and polypropylene (PP), poses critical challenges. While these materials are durable and inexpensive, their improper management after use leads to accumulation of persistent micro- and nanoplastics in soil, deteriorating soil quality, reducing fertility, and potentially threatening food security and human health.[8] Moreover, mechanical film retrieval often results in the loss of nutrient-rich topsoil, further stressing agricultural sustainability. Collection and disposal are also labor-intensive and economically burdensome, resulting in incomplete recovery. Even in regions with advanced recycling systems, such as the European Union, over 30% of agricultural plastic films remained unrecovered as of 2021.[9]

To address these challenges, biodegradable mulch (BDM) films have been developed as sustainable alternatives. BDMs can remain in the field after harvest and are designed to degrade into biomass, water, and gaseous products (*e.g.*, $CO_2$, $CH_4$) through microbial activity under suitable conditions.[10] The performance of such films depends strongly on the feedstock selection and achieving a balance between in-field durability and post-use biodegradability.[11]

Currently, bio-based and biodegradable plastics are dominated by polylactic acid (PLA, >65% market share) and starch-containing polymer compounds (SCPCs, ~10%).[12] Yet, the biodegradation profiles of these materials in soil under ambient conditions (ISO 17556 or ASTM D5988) limit their suitability for mulching applications. For instance, PLA exhibits very limited mineralization under ambient soil conditions (*e.g.*, <1% after 141 days), whereas thermoplastic starch (TPS), a common SCPC, typically degrades too rapidly (~95% mineralization within 136 days), compromising functional lifetime.[13] Furthermore, alignment with Sustainable Development Goals (SDGs 12.2 sustainable resource use, and 12.5 for waste reduction) and the principles of the circular economy necessitates the use of non-edible or waste biomass as a renewable source for BDM production.[14,15]

In this context, dead leaves—an abundant, annually renewable, and non-edible lignocellulosic biomass—represent an attractive feedstock for sustainable BDM production. Despite their widespread availability, fallen leaves are often considered waste. Municipalities expend substantial resources to collect fallen leaves to prevent issues such as eutrophication, drainage blockage, slippery roads or sidewalks, and aesthetic decline.[16] Unfortunately, most collected leaves are incinerated, landfilled, left to decompose, or composted—processes that emit substantial greenhouse gases.[17] As a result, valorizing fallen leaves as BDM feedstock addresses both waste management and sustainable materials development, reducing environmental burdens while promoting circularity.

Lignin-containing nanocellulose fibers (LCNFs), derived from dead leaves, offer a promising solution for sustainable mulch film fabrication. The combination of exceptional characteristics of cellulose nanofibrils (*e.g.*, excellent mechanical strength, well-organized molecular structure, and high biodegradability) and lignin (*e.g.*, thermal stability, hydrophobic and UV protection) makes LCNFs an important building block for outstanding BDM films.[18,19] Nevertheless, LCNFs alone cannot form mechanically robust or flexible films because residual lignin interferes with hydrogen bonding between cellulose fibrils.[20,21] Typically, polymers and additives such as plasticizers, dyes, antioxidants, and ultraviolet (UV) stabilizers are incorporated to achieve desirable film properties. Yet, these additives may leach into soil, and their biodegradability, bioaccumulation potential, and exact content are often insufficiently documented, even in commercial biodegradable films—raising concerns about soil and food chain contamination.[7,22]

Cellulose nanocrystals (CNCs) are highly compatible with LCNFs and can be combined together to produce all-nanocellulose materials with improved mechanical strength, as well as enhanced moisture and oxygen barrier performance.[23,24] However, the inherent brittleness of CNCs limits their practical applications, including in BDM films. To overcome this limitation, the blending of nanocellulose with other polymers such as polylactic acid (PLA), polybutylene adipate-*co*-terephthalate (PBAT), polyvinyl alcohol (PVA), polyethylene glycol (PEG), chitosan, gelatin, and alginate has been investigated.[25–30] Among these, PVA was chosen for this study owing to its non-toxicity, high water solubility, compatibility with nanocellulose, and established biodegradability under certain soil conditions.[31] Nonetheless, achieving simultaneous improvement of mechanical strength, barrier properties, and biodegradability in blended films remains challenging.[15]

Here, we demonstrate a fully water-based, DES-assisted fabrication route to produce biodegradable mulch films from dead leaves. Lignin-containing nanocellulose fibrils (LCNFs) were extracted from them using a hydrated DES composed of citric acid (CA) and choline chloride (ChCl), coupled with ultrasonication. The resulting LCNFs were blended with CNCs, PVA, and glycerol using water as the sole processing medium, and the films were formed *via* evaporation-induced self-assembly. We systematically investigated the physicochemical properties and performance of these films, including tensile strength, moisture barrier performance, hydrophobicity, and UV-blocking capacity. The films' agricultural applicability was also evaluated at the laboratory scale. Finally, we performed soil biodegradation tests to quantify the biodegradation rates (mineralization into $CO_2$) and evaluated the phytotoxicity during crop growth. Our findings demonstrate the feasibility of converting waste biomass into high-performance agricultural mulch films through environmentally benign pretreatment and fabrication strategies, fully aligned with green chemistry principles and the overarching goals of the circular economy and sustainable development.

# 2. Materials and methods

## 2.1. Materials

Dead leaves of sycamore (*Platanus occidentalis*) were collected from the ground on our campus (Korea Advanced Institute of Science & Technology, KAIST) and near Gapcheon riverside (Daejeon, Republic of Korea) in November 2023. The collected leaves were thoroughly washed under tap water, air-dried under ambient laboratory conditions, and then ground into 100–250 μm powders. Prior to storage, the powder was oven-dried at 60 °C for 24 h to reduce moisture content, until reaching constant mass. The main chemical compositions (cellulose, hemicellulose, and lignin) are summarized in Table S1. Cellulose nanocrystals (CNCs) were purchased from CelluForce (Quebec, Canada; grade NCV100–NASD90) as spray-dried powder with a particle size of approximately 127 nm, as reported by the supplier.

Polyvinyl alcohol (PVA) powder ($M_w$ = 89 000–98 000, >99% hydrolyzed), choline chloride (≥98%), citric acid (≥99.5%), glycerol (≥99.5%), α-cellulose, cadmium chloride hemi(pentahydrate) (79.5–81.0%), sulfuric acid (95–98%), anhydrous calcium chloride (≥99.9%), potassium phosphate monobasic ($KH_2PO_4$), magnesium sulfate ($MgSO_4$), sodium nitrate ($NaNO_3$), urea, ammonium chloride ($NH_4Cl$), and glutaraldehyde solution (Grade I) were purchased from Sigma-Aldrich Chemical Co. (St Louis, MO, USA). Anhydrous ethanol (≥96%) was obtained from Duksan Pure Chemicals (Republic of Korea). Low-density polyethylene (LDPE, LB7500N, LG Chem, Republic of Korea) was kindly provided by Yonsei University. Deionized (DI) water was used throughout this study.

## 2.2. Synthesis of the LCNFs

ChCl was first dried at 60 °C for 24 h to remove residual moisture and then stored in a desiccator to maintain its dryness. ChCl, CA, and water were then mixed at a mass ratio of 1 : 3 : 1 and stirred at room temperature for 2 h to obtain a homogeneous and colorless liquid (DES).

Dead-leaf powder of sycamore (4 g) was added to a round-bottom flask containing 100 mL of prepared DES. The flask was then attached to a reflux condenser to retain water content and placed in an oil bath at 100 °C under stirring at 500 rpm for 3 h. Subsequently, 100 mL of ethanol was added immediately to quench the reaction, and the flask was placed in an ice bath to cool down. Afterward, the solid slurry was collected and thoroughly rinsed with DI water five times by centrifugation (4000 rpm, 5 min). The slurry was fully transferred into a beaker and DI water was added until a suspension of 60 g (3 wt%) was obtained. The suspension was subjected to ultrasonic treatment (800 W, 5 s pulse, 1 s off) in an ice bath. Finally, an LCNF suspension was obtained and stored at 4 °C for further use. The yield of LCNFs, based on the dry weight of the collected slurry, was approximately 45% (1.8 g). The detailed composition of LCNFs is provided in Table S1.

## 2.3. Fabrication of biodegradable mulch (BDM) film

Initially, a 6 wt% CNC suspension was prepared by adding the CNC powder to water through a sieve (250 μm) while stirring vigorously (1000 rpm) to ensure uniform dispersion. The suspension was then ultrasonicated (800 W, 5 min, 5 s pulse, 1 s off), and stirred at 700 rpm for 48 h, with the beaker tightly covered with parafilm. This prolonged mixing step improves CNC hydration and prevents micro-agglomeration, which is typical in spray-dried CNC powders. Afterward, the suspension underwent an additional 30 min of ultrasonication to remove any remaining aggregates and was kept at 4 °C. Subsequently, the LCNF suspension was first pre-mixed with CNCs at various dry weight ratios, and samples were designated as LCNF, LCNF70CNC30, LCNF50CNC50, LCNF30CNC70, and CNC. Film-casting suspensions were prepared by adding a fixed amount of glycerol (Gly) as a plasticizer using ultrasonication. Glycerol was added at 31.25% by weight relative to the dry mass of LCNF and CNC.

LCNF50CNC50 (or LANC) suspension was selected for further modification with PVA to improve flexibility, which is required for BDM films. A 6 wt% PVA solution was prepared by dissolving PVA powder in water under stirring in a water bath at 90 °C for 1 h. BDM films were then fabricated by adding PVA at different ratios relative to the dry mass of LCNF and CNC. The detailed compositions of the BDM films are presented in Table 1. All suspensions were cast on polystyrene Petri dishes ($d$ = 90 mm) and dried at room temperature. The thickness of all cast films was controlled to approximately 0.1 mm. A schematic illustration outlining the detailed procedure (Fig. S1) and underlying mechanisms (Fig. 1) for each step involved in the fabrication of the BDM films is presented.

## 2.4. Characterization of LNCF/CNC and LANC/PVA films

**2.4.1. Scanning electron microscopy (SEM).** The morphological structure of the samples was observed by field emission SEM (FE-SEM, SU5000, Hitachi, Japan; FEI Quattro S, Thermo Scientific, USA) at 10 kV. Cross-sectional images were prepared by cryo-fracturing the samples in liquid nitrogen and inserting them into a holder. All samples were coated with platinum prior to analysis.

To observe the microbial community on the film's surface as part of the soil biodegradation test (see details in section 2.4.10), the samples were cleaned in an ultrasonic bath (NXPC-B3010S, KODO, Republic of Korea) for 3 × 15 seconds to ensure complete removal of surface residues. Subsequently, each sample was transferred into a 2.5 vol% glutaraldehyde solution and soaked in the dark for 24 h to preserve the cell structure of the microorganism. The film was thoroughly cleaned with 70 vol% ethanol solution to remove residual glutaraldehyde and dried at room temperature before analysis.

**2.4.2. Fourier-transform infrared (FT-IR) spectroscopy.** The FT-IR spectra of samples were recorded using a Nicolet iS50 FT-IR spectrometer (Thermo Fisher Scientific, USA) operating in attenuated total reflectance (ATR) mode. The scans were per-

**Table 1** Relative compositions of the LCNF/CNC and LANC/PVA films

| Samples | Dispersion solids content (% w/v) | LCNF (g) | CNC (g) | Gly (mL) | LCNF in film (wt%) | CNC in film (wt%) | Gly in film (wt%) |
|---|---|---|---|---|---|---|---|
| LCNF | 3.94 | 3 | 0 | 0.75 | 76.2 | 0 | 23.8 |
| LCNF70CNC30 | 3.94 | 2.1 | 0.9 | 0.75 | 53.3 | 22.9 | 23.8 |
| LCNF50CNC50 | 3.94 | 1.5 | 1.5 | 0.75 | 38.1 | 38.1 | 23.8 |
| LCNF30CNC70 | 3.94 | 0.9 | 2.1 | 0.75 | 22.9 | 53.3 | 23.8 |
| CNC | 3 | 0 | 3 | 0 | 0 | 100 | 0 |

| Samples | Dispersion solids content (% w/v) | LANC[a] (g) | PVA (g) | Gly (mL) | LANC in film (wt%) | PVA in film (wt%) | Gly in film (wt%) |
|---|---|---|---|---|---|---|---|
| LANC25PVA75 | 3.94 | 3 | 2.25 | 0.75 | 48.4 | 36.4 | 15.2 |
| LANC50PVA50 | 3.94 | 3 | 1.5 | 0.75 | 55.2 | 27.6 | 17.2 |
| LANC75PVA25 | 3.94 | 3 | 0.75 | 0.75 | 64 | 16 | 20 |
| PVA | 3 | 0 | 3 | 0 | 0 | 100 | 0 |

[a] LANC denotes the simplified code name derived from LCNF50CNC50.

formed with a resolution of 1 $cm^{-1}$ and a scan speed of 64 cm $s^{-1}$ in the range of 4000 $cm^{-1}$ to 400 $cm^{-1}$.

**2.4.3. X-ray diffraction (XRD).** The XRD pattern of samples was acquired by a high-resolution X-ray diffractometer (SmartLab, Rigaku, Japan) with Cu $K\alpha_1$ radiation ($\lambda$ = 0.154 nm) in the $2\theta$ range of 5–50° at a speed of 5° $min^{-1}$. The crystallinity index (CrI) of the samples was estimated from XRD patterns using a peak deconvolution method[32] as follows:

$$\mathrm{CrI}\,(\%) = \frac{A_{\mathrm{cr}}}{A_{\mathrm{cr}} + A_{\mathrm{am}}} \times 100 \quad (1)$$

where $A_{cr}$ and $A_{am}$ indicate the areas of all the crystalline and amorphous regions, respectively. These values were obtained computationally with OriginPro software.

**2.4.4. Thermogravimetric analysis (TGA).** The thermal decomposition behavior of the samples was assessed using thermogravimetric analyzers (TG209 F1 Libra, Netzsch, Germany; TGA2, Mettler Toledo, Switzerland) in the temperature range of 25–800 °C, with a heating rate of 10 °C $min^{-1}$ under an $N_2$ atmosphere.

**2.4.5. Density and porosity estimation.** The thickness of the films was measured using a thickness tester (Quick-Mini, Mituyoko, Japan) in accordance with the ISO 534:2011 standard. Bulk density was calculated by dividing the sample weight by total volume, and true or skeletal density was obtained from use of a helium gas pycnometer (AccuPyc II 1340, Micromeritics, USA). Theoretical porosity of the films was then calculated based on bulk and skeletal densities following the equation:

$$\mathrm{Porosity}\,(\%) = \frac{\rho_{\mathrm{skeletal}} - \rho_{\mathrm{bulk}}}{\rho_{\mathrm{skeletal}}} \times 100 \quad (2)$$

**2.4.6. Mechanical testing.** The tensile strength, Young's modulus and elongation at break of the films were evaluated on a universal testing machine (Instron 5848, Instron, UK) equipped with a 500 N load cell. The testing was conducted in triplicate, at a speed of 50 mm $min^{-1}$ under controlled temperature (23 °C) and 45% relative humidity (RH) conditions. Three specimens of each sample were tested.

**2.4.7. UV–vis spectroscopy.** The transmittance spectra of the samples were measured using a UV-vis/NIR spectrophotometer (Lambda 1050, PerkinElmer, USA) in the wavelength range of 200–800 nm. Film transparency was determined by observing the transmittance at a wavelength of 550 nm. The direct solar transmittance in the photosynthetically active radiation (PAR) range (400–700 nm, $\tau_{\mathrm{PAR}}^{\mathrm{direct}}$) was calculated using eqn (3).[33] Meanwhile, the UVA and UVB shielding capacity values were quantified using eqn (4) and (5), respectively:[34]

$$\tau_{\mathrm{PAR}}^{\mathrm{direct}} = \frac{\sum_{400}^{700} S(\lambda)\Delta\lambda\tau(\lambda)}{\sum_{400}^{700} S(\lambda)\Delta\lambda} \quad (3)$$

$$\mathrm{UVA\ blocking}\,(\%) = 100 - \frac{\int_{320}^{400} \tau(\lambda)\mathrm{d}\lambda}{\int_{320}^{400} \mathrm{d}\lambda} \quad (4)$$

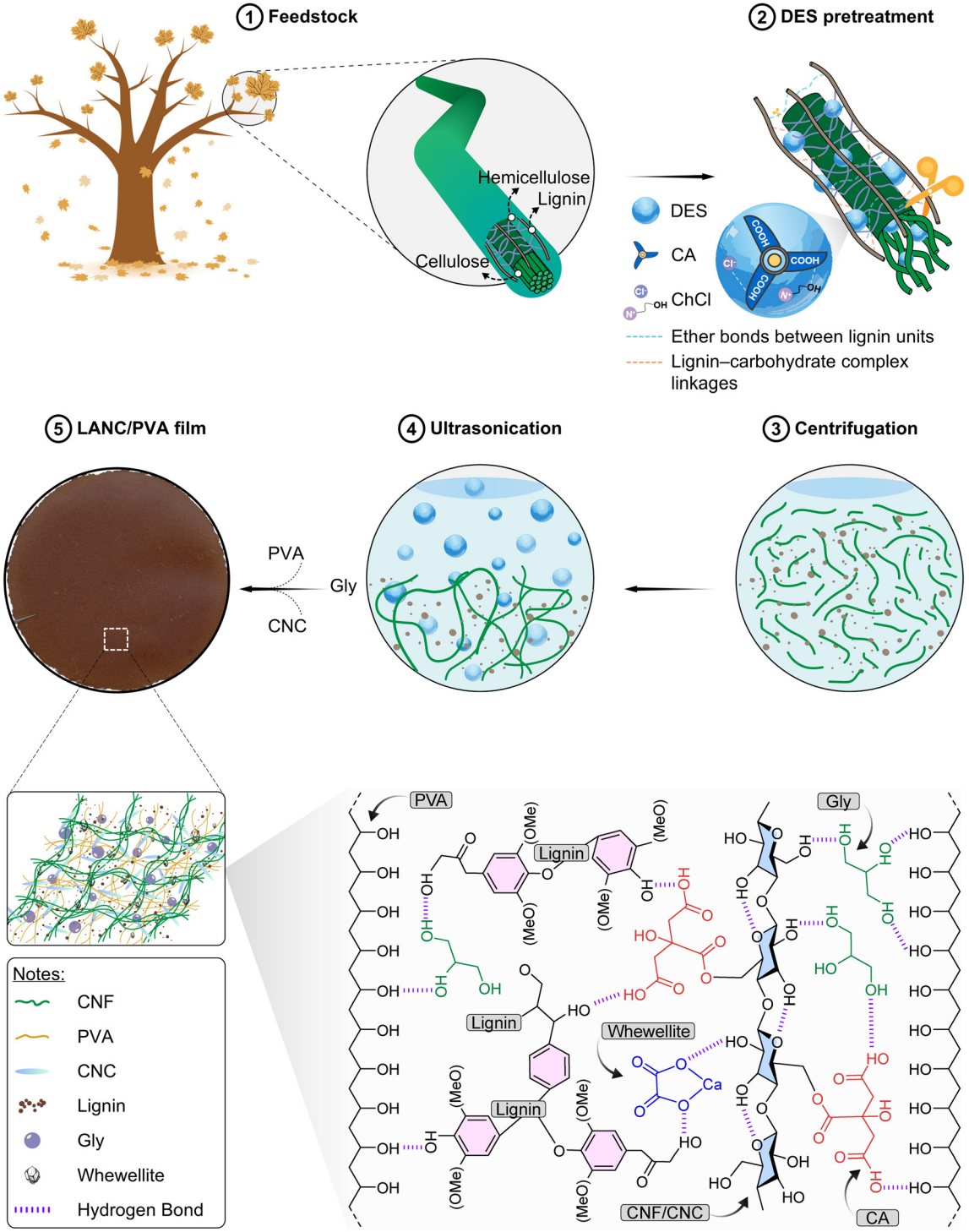


**Fig. 1** Schematic representation of the fabrication process and self-assembly mechanism of BDM films *via* complex hydrogen-bonding interactions.

$$\text{UVB blocking}\,(\%) = 100 - \frac{\int_{280}^{320} \tau(\lambda)\mathrm{d}\lambda}{\int_{280}^{320} \mathrm{d}\lambda} \quad (5)$$

where $\tau(\lambda)$ is the average spectral transmittance of the film, $\Delta\lambda$ is the wavelength interval (10 nm), $S(\lambda)$ is the relative spectral distribution of solar radiation obtained from the ISO 9845-1:2022 standard, and the corresponding values $S(\lambda)\Delta\lambda$ were re-calculated following the ISO 9050:2003 standard. Additionally, $\mathrm{d}\lambda$ represents the bandwidth, and $\lambda$ denotes the wavelength.

**2.4.8. Contact angle measurements.** A contact angle analyzer (SEO Phoenix, Surface Electro Optics., Republic of Korea)

was used for the water contact angle (WCA) measurements. The WCA values were reported by analyzing images at 60 s after applying 5 μL droplets.

**2.4.9. Water vapor permeability (WVP).** The WVP of the samples was determined using a slightly modified gravimetric desiccant method, as outlined in the ASTM E96/E96M-24a standard. A round-shaped film ($d$ = 2.1 cm) was placed on a sealed black vial with an open-top cap ($d$ = 1.5 cm), which contained approximately 5 g of anhydrous $CaCl_2$. This setup was then placed in a climatic chamber (JSCH-100CPL, JS Research Inc., Republic of Korea) maintained at 50% RH and 23 °C. The weights of the vials were recorded at 4 h intervals for 48 h. The collected values were then plotted against time, and the slope of the resulting curve was obtained through linear regression. Finally, the water vapor transmission rate (WVTR) and WVP were calculated as follows:

$$\mathrm{WVTR} = \frac{\Delta m}{\Delta t} \times \frac{1}{A} \tag{6}$$

$$\mathrm{WVP} = \frac{\mathrm{WVTR} \times d}{\Delta P} = \frac{\mathrm{WVTR} \times d}{S \times (R_1 - R_2)} \tag{7}$$

where $\Delta m$ represents the change in weight (g); $\Delta t$ is the time interval (h); $A$ is the exposed area of the film ($m^2$); $d$ is the film thickness (m); $\Delta P$ is the vapor pressure difference between the two sides of the film (Pa); $R_1$ and $R_2$ are the RH in the test chamber and inside the vial (50% and 0%, respectively); and $S$ is the saturation water vapor pressure (Pa), which is 2811.1 Pa at 50% RH and 23 °C.[35]

**2.4.10. Biodegradation rate in soil.** The biodegradation rates of mulch film samples were investigated based on carbon mineralization into $CO_2$ using a respirometer equipped with a non-dispersive infrared $CO_2$ sensor (ECHO Instruments, Slovenia, EU), following the ISO 17556:2019 standard. Because mulch films are intended to remain in the field after harvest, biodegradation was evaluated in natural soil under aerobic conditions; aquatic and marine biodegradation were not assessed in this study. Initially, soil was collected from the forest within the campus of KAIST and from near Gapcheon riverside (Fig. S2) to obtain heterogeneous microbial inoculum in pristine environments. The soil was air-dried under ambient conditions for 3 days, then sieved through a 2 mm mesh and mixed in a 50 : 50 wt% ratio. The water content was measured using a moisture analyzer (WiseWeigh WBA-110M, SciLab, Republic of Korea), and the final soil moisture content was 40% of the maximum water-holding capacity (44%). A nutrient solution containing 0.2 g of $KH_2PO_4$, 0.1 g of $MgSO_4$, 0.4 g of $NaNO_3$, 0.2 g of urea, and 0.4 g of $NH_4Cl$ per kg of soil was added to enrich the soil before incubation. Subsequently, 10 g of sample (850–1000 μm particle size) was thoroughly mixed with 800 g of soil. The resulting mixture was then transferred into the reactor vessel and incubated within the respirometer chamber, maintained at a constant temperature of 25 ± 0.5 °C in the dark.

The incubation was continued until $CO_2$ evolution approached a plateau (~120 days). Cellulose powder served as a positive control, LDPE film as a negative control, and soil without additional substrate as a blank control. Measurements included average produced $CO_2$ from each vessel, net $CO_2$ production (calculated as the difference between produced $CO_2$ from samples and blank controls), and biodegradation levels (%). Standard deviations were computed cumulatively. The biodegradation level (mineralization) was calculated following the methodology described in ISO 17556:2019, as follows:

$$\text{Mineralization}\ (\%) = \frac{\sum m_{\mathrm{CO_2,s}} - \sum m_{\mathrm{CO_2,b}}}{\mathrm{ThCO_2}} \times 100 \tag{8}$$

where $m_{\mathrm{CO_2,s}}$ and $m_{\mathrm{CO_2,b}}$ represent the amount of $CO_2$ produced in the sample and blank vessels, respectively (mg). $ThCO_2$ is theoretical maximum $CO_2$ production, calculated from the carbon content of the samples, which was determined using an elemental analyzer (EA 1112, Thermo Fisher Scientific, USA; Table S2).

**2.4.11. Ecotoxicity test.** The potential ecotoxicity effects of samples on seed germination and plant growth were evaluated according to the OECD 208 guidelines using a plant incubation chamber and plant seed-kit modules (Tiiun, LG Electronics, Republic of Korea). A commercially available loamy soil (Biophilia Co., Republic of Korea), composed of coke peat, peat moss, perlite, zeolite, clay sand, humus, and fermented bark, with a water-holding capacity of 50.2 ± 3.4% and pH ranging from 6.5 to 7.1, was selected as the substratum. No additional nutrients were provided to the plants during the test period. Film samples (5 mg, 850–1000 μm particle size) were thoroughly mixed with soil (495 mg, <2 mm), and the resulting mixture was filled into each hole of the test kit (5 holes in total). Each hole was fabricated with a sponge designed for water absorption and retention. Subsequently, two seeds of ryegrass (*Lolium multiflorum*) or one seed of tatsoi (*Brassica rapa*) were planted into each hole. DI water (10 mL) was then slowly added until excess water seeped out from the bottom of the test kit. $CdCl_2$ (5 mg per 495 mg of soil, denoted as $CdCl_2$-1%), LDPE film, and pristine soil served as the positive, negative and blank controls, respectively.

All Tiiun modules were incubated under controlled diurnal photoperiod conditions consisting of a 16-hour light cycle (intensity: 5500 ± 500 lux) followed by an 8-hour dark cycle. Temperature and relative humidity conditions were maintained at 20.5 ± 3.2 °C and 58.4 ± 14.4% RH, respectively, and continuously monitored using an RC-4HC data logger (Elitech, USA; Fig. S3). DI water was manually replenished by pouring 50 mL into the test kit holder—once per week for the first three weeks, and every three days thereafter. The germination rate, shoot fresh mass, and shoot length were measured after 14 days for ryegrass and after 55 days for tatsoi. Fresh biomass weight and shoot length measurements were conducted immediately after cutting the roots.

**2.4.12. Moisture retention behavior.** The moisture retention capability of the LANC50PVA50 film was investigated

 

through a pot experiment designed to mimic practical field application. A light-shielding amber vial was filled with 10 g of commercial soil (as in the ecotoxicity test), followed by the slow addition of 12 mL of DI water. Next, one seed of ryegrass was sown at a depth of 0.5 cm beneath the topsoil surface. A round-shaped LANC50PVA50 film ($d$ = 2.1 cm) with a hole in the center ($d$ = 0.4 cm) was placed on an open-top cap ($d$ = 1.5 cm) to cover the vial. This hole mimics openings in agricultural mulch films for plant emergence. Additional vial setups included: (1) a vial without film but containing a seed; (2) a vial covered with film (with a hole) but without a seed; (3) a vial covered with film (without a hole) for comparison; and (4) a vial tightly sealed with a PE septa-lined cap, which served as a blank sample. Each vial type was prepared in quintuplicate, and the experiment was conducted in triplicate.

Subsequently, all vials were placed into the incubation chamber under similar conditions to those used in the ecotoxicity test. The germination rate, shoot fresh mass, shoot length, and moisture content were measured after 14 days. No additional nutrients or water were provided to the plants during the test period.

**2.4.13. Statistical analysis.** All measurements were performed in triplicate, and the results are reported as averages ± standard deviations. Statistical analyses were conducted using OriginPro 2025. One-way analysis of variance (ANOVA) followed by Tukey's *post hoc* test was employed to determine significant differences among samples, with a significance threshold of $P < 0.05$ at a 95% confidence level.

# 3. Results and discussion

## 3.1. Characterizations of LANC/PVA mulch films

**3.1.1. Textural and morphological properties.** The top-view image of an LCNF film (Fig. 2A) exhibited a loose and rough surface morphology with nonuniform and irregular lignin flakes trapped within a nano/micro-cellulose fibril network. In contrast, the PVA and CNC films displayed smooth, uniform, and flat surfaces with no visible cracks or voids (Fig. S4). As CNC and/or PVA content increased in the LCNF film, its top surface became more compact, denser, smoother, and more uniform, resulting in a significant decrease in roughness ($R_a$) values from 150 nm to 72.4 nm and 22.3 nm for LCNF, LANC, and LANC50PVA50, respectively (Fig. 2B). These densification effects are consistent with CNC's rod-like morphology enabling tighter packing and PVA's film-forming behavior reducing inter-fibrillar voids. Similarly, cross-sectional images of LANC and LANC50PVA50 revealed fewer visible pores in the internal structure upon PVA addition. These changes in both top and cryo-fractured surfaces are attributed to the ability of CNC and PVA to fill the voids within the LCNF network, leading to a considerable reduction in porosity (Table S3 and Fig. S4). These observations also suggest strong interfacial compatibility, likely arising from extensive hydrogen bonding among hydroxyl-rich LCNF, CNC, and PVA.

**3.1.2. Chemical structure.** The changes in chemical structure and interactions between components in the films were thoroughly examined using FT-IR. Specifically, the spectrum of LCNF (Fig. S5) exhibited a distinctive peak at 1730 $cm^{-1}$,

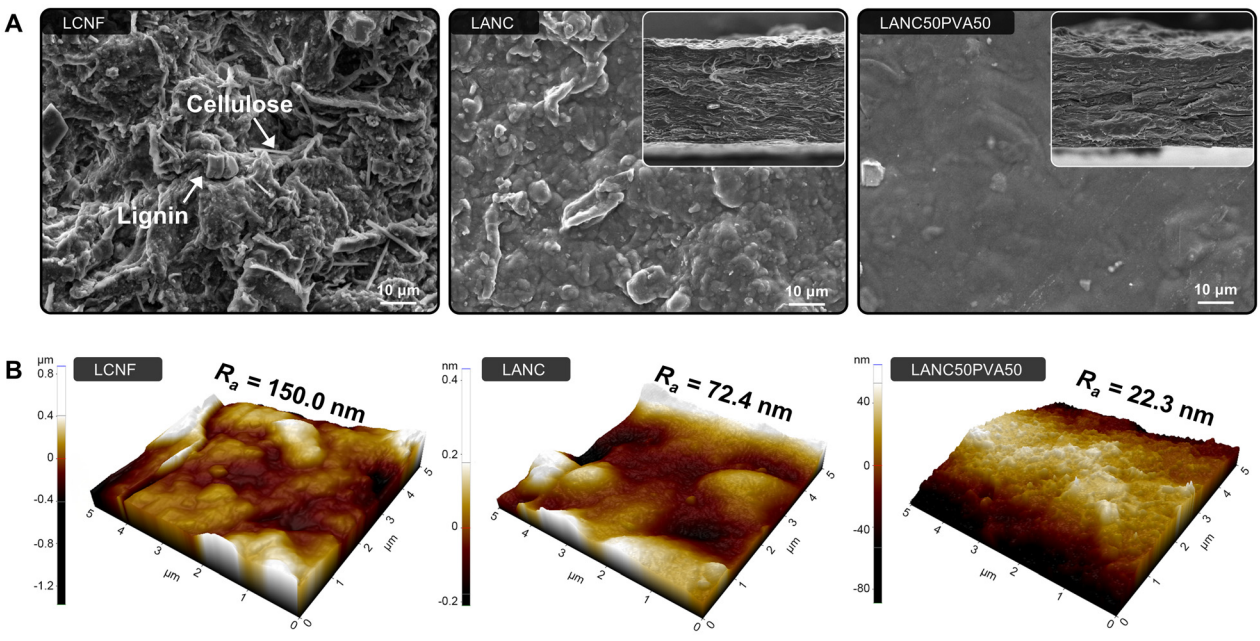


Fig. 2 (A) SEM images of LCNF, LANC and LANC50PVA50 films. Cross-sectional images of LANC and LANC50PVA50 films are shown in the insets. (B) AFM images of LCNF, LANC, and LANC50PVA50 films.

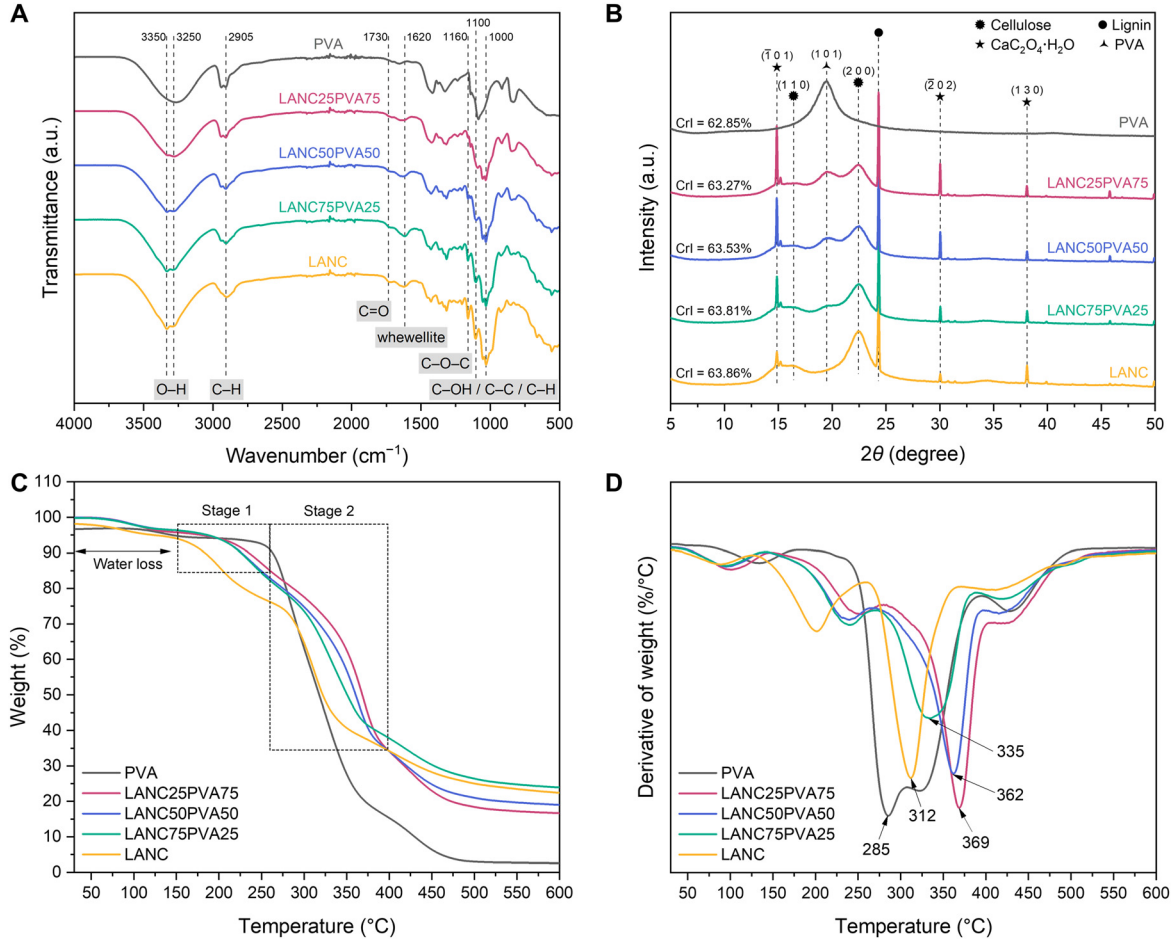


**Fig. 3** (A) FTIR spectra, (B) XRD patterns, (C) TGA curves, and (D) DTG curves of LANC/PVA films of different ratios.

corresponding primarily to O–C═O stretching in esterified carboxyl groups formed during DES pretreatment or to the ferulic or *p*-coumaric acid moieties in lignin.[36] The presence of residual lignin in the LCNF is further clarified by the C═C symmetric stretching vibration at 1620 $cm^{-1}$ and a weaker band at 1515 $cm^{-1}$, corresponding to the aromatic skeleton of lignin.[18] The broad intensity around 1620 $cm^{-1}$ also originates from the C═O asymmetric stretching vibration of the oxalate molecules ($C_2O_4^{2-}$) of whewellite,[37] as well as from bound water due to the water-trapping nature of cellulose,[38] resulting in a broader and more intense band in LCNF compared to CNC and extracted cellulose (Fig. S6). In addition, the peak at 1000 or 1100 $cm^{-1}$ is related to the C–OH, C–C, and C–H vibrations, while the peak at 1160 $cm^{-1}$ is related to asymmetrical C–O–C stretching vibrations, a feature typical of cellulose I.[17,23] The introduction of CNC into LCNF did not significantly alter the overall appearance of the FTIR spectra, as CNC contains the same functional groups as cellulose. However, minor changes observed around 3250 $cm^{-1}$ and 3350 $cm^{-1}$ likely arise from enhanced intermolecular hydrogen bonding among CNC particles and between CNC and LCNF.[23] Moreover, the further addition of PVA contributed to changes in the broad band at 3000–3750 $cm^{-1}$ and the peak at 2905 $cm^{-1}$, assigned to O–H and symmetrical C–H stretching vibrations, respectively (Fig. 3A). This phenomenon is likely associated with the formation of inter- and intramolecular hydrogen bonding among PVA, cellulose, lignin, whewellite and glycerol.[39,40]

**3.1.3. XRD analysis.** The XRD patterns of leaf powder and LCNF film (Fig. S5) revealed the crystalline structure of the cellulose I allomorph, with peaks at 2$\theta$ values of approximately 14.8°, 16.5°, and 22.6°, corresponding to the (1$\bar{1}$0), (110) and (200) crystal planes, respectively. The presence of lignin and whewellite was also demonstrated by various peaks located in the range of 10–50°.[17,41] This similarity suggests that the treatment process did not disrupt the crystalline structure of cellulose, but rather removed hemicellulose and amorphous cellulose regions,[42] as evidenced by the increase in CrI from 30.7% to 37.6%. This preservation of cellulose I crystallinity indicates that the DES/ultrasonic pretreatment selectively removed amorphous polysaccharides without altering the underlying crystalline microfibril structure. Moreover, the XRD peaks remained nearly unchanged except for the crystalline region, when CNC was introduced into LCNF, as CNC's crystallinity (CrI = 87.5%) is significantly higher than that of LCNF (CrI = 37.6%).

Upon incorporating PVA into the LANC matrix, a new diffraction peak appeared at $2\theta \sim 19.6°$ (Fig. 3B), a characteristic feature of semicrystalline PVA, confirming its successful incorporation into the composite structure.[43] Additionally, the crystalline index of LANC/PVA composites did not change appreciably, as the crystalline indices of LANC and PVA are quite similar (63.86% and 62.85%, respectively). However, the intensity of the PVA diffraction peaks became clearly weaker with increasing LANC content, suggesting partial loss of its ordered structure, potentially due to the formation of new hydrogen bonds between PVA and other matrix components. This hypothesis is further supported by the rise in the intensity of diffraction peaks corresponding to lignin and whewellite. It is important to note that the interactions between lignin, whewellite, and cellulose occurred at the surface, and thus did not influence the robust crystalline lattice within the cellulose structure, but rather physically diminished the intensity of their diffraction peaks.[44,45]

**3.1.4. Thermal behavior.** The TGA and DTG thermograms were employed to evaluate the thermal stability and degradation behavior of all samples. The TGA curves (Fig. 3C, D and Fig. S5) showed that all samples underwent a small weight loss (5–8%) associated with the evaporation of moisture below 150 °C, followed by two main stages of decomposition between 200 and 600 °C. The first stage of thermal degradation began at around 180 °C, primarily attributed to the decomposition of hemicellulose, lignin, and glycerol in all samples except for pure PVA and CNC. In the second stage, which began at approximately 260 °C, cellulose, PVA, and their combinations with other components started to decompose as hydrogen bonds were cleaved, continuing until most components were converted into char around 450 °C. It should be noted that the pyrolysis of lignin polymers started earlier but lasted longer than that of cellulose and hemicellulose due to its structural complexity.[46] The combination of CNC and LCNF improved the thermal stability of their composites below 280 °C and lowered their decomposition above 280 °C compared to LCNF or CNC alone, indicating better thermal stability in samples with higher lignin (LCNF) content (Table S4).

Interestingly, as shown in the DTG plots (Fig. 3D) and summarized values (Table S4), although $T_{onset}$ and $T_{max}$ of neat PVA film were lower than those of the LANC film, their composites exhibited significantly higher values with increasing PVA content. These results suggest that the incorporation of PVA considerably enhanced the thermal endurance of the LANC/PVA composites. This enhancement can be attributed to the formation of stronger and denser inter- or intramolecular hydrogen bonds between PVA, cellulose, lignin, whewellite, and glycerol, facilitated by the increased presence of –OH groups in PVA, ultimately leading to the creation of a more stable and complex network.[19] Moreover, it has also been reported that the high compatibility between PVA and LANC enhanced the stability of their composite interfacial adhesion,[43] while lignin can form a thermally insulating char layer during the heating process.[47] This combination contributes to the retardation of the LANC/PVA film decomposition at high temperatures, as evidenced by the higher percentage of charred residue, as shown in Table S4.

### 3.2. Performance of LANC/PVA mulch films

**3.2.1. Mechanical properties.** Stress–strain curves of the LANC/PVA and LCNF/CNC films were evaluated to investigate the mechanical behavior of films (Fig. 4A and Fig. S7, respectively). The maximum tensile strength, strain at break, and Young's modulus (stiffness) are also summarized (Table S5). LCNF films exhibited a significant enhancement in tensile strength upon CNC addition to their matrix, but showed limited flexibility due to the brittle nature of CNC.[48] Therefore, a ratio of LCNF and CNC (50 : 50, LANC) was selected for further modification as in previous studies.[23,24,49] As predicted, the addition of PVA further improved the ultimate mechanical properties of LANC/PVA films, for example, LANC50PVA50 films exhibited notable increments in tensile strength (2×), strain at break (3×), and stiffness (1.1×) in comparison with non-modified LANC. The observed reinforcement likely stems from CNC's high intrinsic modulus and its ability to form a rigid percolation network within the LCNF matrix. These drastic improvements can presumably be attributed to: (1) its denser and smoother structure with low percentage of porosity (Fig. S4 and Table S3); (2) the good interfacial adhesion properties and compatibility between LANC and the PVA matrix;[50] and (3) the complex interaction of the percolation network (CNF/CNC), lignin, and glycerol with the PVA matrix through inter-/intramolecular hydrogen bonding or weak van der Waals forces.[43]

**3.2.2. UV-blocking properties.** The UV–vis spectra of all films were measured to evaluate their transparency and UV-protecting properties. As shown in Fig. 4B, the transmittance of pure PVA was considerably high in both the visible and UV regions, indicating apparently its limited role in UV protection. On the other hand, LANC films effectively blocked broad-spectrum ultraviolet radiation, with over 99.9% absorption of medium-wavelength UVB (280–320 nm) and nearly 100% of long-wavelength UVA (320–400 nm). This excellent UV-shielding capability arises from the presence of lignin, which is well-known for its inherent UV-absorbing properties due to its richly conjugated aromatic functionalities, such as phenolic groups, ketones, and other chromophores.[51,52] Interestingly, incorporating a high content of PVA (75 wt%) into LANC did not affect its excellent UV protection, as evidenced by the unchanged 0% transmittance in the 200–400 nm range. Presumably, the densification of PVA and LANC creates a strong hydrogen bond network in their composite films, stabilizes the functional group of lignin and ensures their uniform distribution in the matrix, preserving the UV-resistant properties.[53]

The optical properties and photosynthetically active radiation (PAR) values were investigated to assess the light transmission of LANC/PVA films within the 400 to 700 nm wavelength, which plants utilize for photosynthesis. Fig. 4C shows the optical transmittance of LANC films as a function of PVA concentration in the visible range, while no significant change

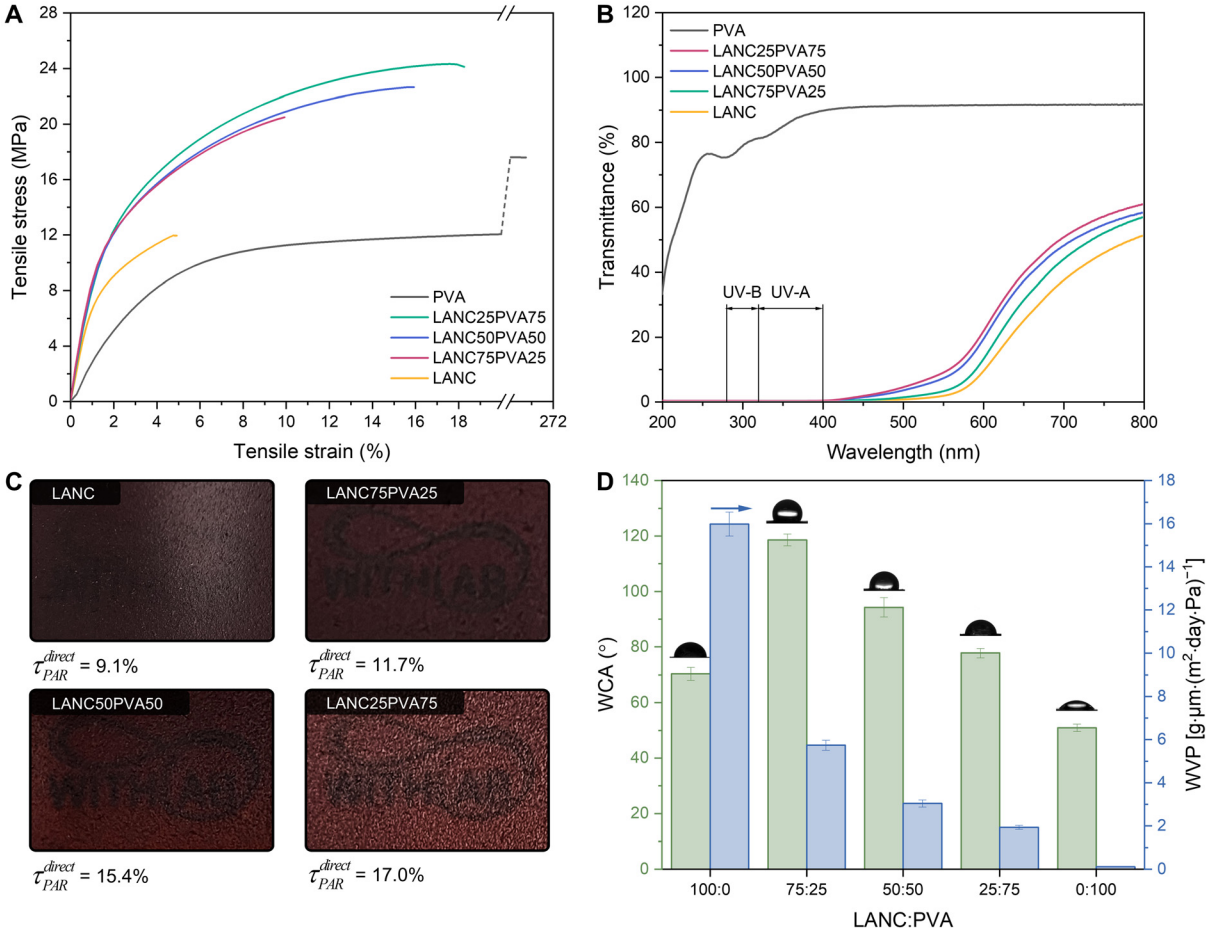


**Fig. 4** (A) Typical stress–strain curves, (B) UV–vis spectra, (C) photographs and values of the direct transmission coefficient in the PAR region, and (D) water contact angle (WCA) and water vapor permeability (WVP) of LANC/PVA films.

was observed in the UV region. The film's appearance became slightly brighter with the addition of PVA, though it remained difficult to perceive objects through it due to the initially extremely high opacity of LANC. Furthermore, the PAR light transmittance showed minimal change with higher PVA content; for instance, only 15.4% of light passed through the LANC50PVA50 film compared to 9.1% for LANC. This low PAR transmittance suggests that the LANC50PVA50 film is suitable as a functional analogue to commercial black mulch films, which are designed to strongly suppress visible light in order to inhibit weed growth and retain heat during the autumn and winter seasons.

**3.2.3. Water contact angle.** The surface hydrophobicity of the films was evaluated through WCA measurements, with the average values presented graphically in Fig. 4D. PVA films exhibited a low WCA (50.9 ± 1.3°), which is apparently attributed to their hydrophilic nature caused by the abundant –OH groups on their skeleton. In contrast, its composite films were remarkably more hydrophobic than those of LANC and PVA, as evidenced by eminently higher WCA values (77.8 ± 1.3° to 118.6 ± 2.1°). This increased hydrophobicity is expected due to the amphiphilic nature of the lignin, which contains fewer hydroxyl groups and more hydrophobic groups such as phenolics,[19] as well as the presence of aromatic moieties in lignin,[54] as confirmed by the FTIR spectra shown in Fig. 3A. In addition, polymer-chain rearrangement during drying may orient hydrophobic moieties toward the film–air interface, increasing the apparent surface hydrophobicity. Furthermore, the interactions between all components also played a crucial part in increasing the hydrophobicity of LANC/PVA films. As demonstrated by various analyses in the characterization section, lignin, cellulose, whewellite, glycerol, and PVA were mutually hydrogen-bonded. These intermolecular interactions may promote surface enrichment of hydrophobic segments from PVA, cellulose, and lignin, thereby reducing the availability of polar Lewis sites and lowering the surface energy of the films.[48] Interestingly, LCNF film exhibited the poorest hydrophobicity (WCA ~ 20°), despite having the highest lignin content. One possible explanation for this can be derived from their loose structure and high porosity (45%, Fig. S4 and Table S3), which allows water to easily penetrate the surface.

**3.2.4. Water vapor permeability.** WVP is a foremost factor that determines a mulch film's water moisture retention capability for effective crop production. Fig. 4D shows that

 

LANC25PVA75 films exhibited the highest water vapor barrier, with the lowest WVP value of 1.93 ± 0.09 g μm ($m^2$ day Pa)$^{-1}$ among LANC/PVA composites. Further increasing the percentage of LANC to 50% and 75% in the composites resulted in a significant accretion of WVP, by about one-and-a-half and three times to reach 3.04 ± 0.17 and 5.74 ± 0.23 g μm ($m^2$ day Pa)$^{-1}$, respectively, indicating reduced moisture barrier performance of films with higher LANC proportions. One possible explanation for this trend is the structural change in materials, shifting from a more compact, low porosity framework to a looser, high porosity structure, as demonstrated in Fig. 2A, B and Table S4. Additionally, there may be increased phase separation between PVA and LANC.[55]

Interestingly, although PVA is a polyhydroxy polymer with inherently hydrophilic properties (WCA = 50.9°), it displayed markedly superior water vapor barrier behavior (WVP = 0.11 ± 0.003 g μm ($m^2$ day Pa)$^{-1}$) compared with the LANC/PVA composite films, which exhibited more hydrophobic surfaces with WCAs of 77.8–118.6°. Although PVA is hydrophilic, its high cohesive energy density and tight chain packing create a substantial diffusion barrier to water vapor,[56] which is even higher than that for non-polar polymers such as polypropylene or polystyrene.[57] This property hinders the movement of water vapor molecules from one side to the other side of the film, especially under low temperature and RH conditions.[58] Similar WVP values for pure PVA of 0.06 g μm ($m^2$ day Pa)$^{-1}$ under the same testing conditions (23 °C and 50% RH) have also been reported.[59]

Overall, film porosity was revealed to exhibit a strong correlation with moisture-barrier performance, often outweighing the effects of crystallinity or surface hydrophobicity. Specifically, films with fewer porous, denser networks and highly random structures were able to maintain a high degree of tortuosity under low temperature and RH conditions, making it difficult for water molecules to penetrate or diffuse through the layers. This created a powerful water-resistant barrier, helping to prevent soil moisture loss in agricultural mulch film applications. These findings align with those of other studies demonstrating that pore volume is the dominant mechanism in controlling vapor permeability.[60,61] An additional noteworthy observation is that LANC/PVA films exhibited strong potential for use as mulching films (Table S6).

**3.2.5. Biodegradability.** To explore the biodegradation of the LANC50PVA50 mulching film, we investigated the mineralization of its internal carbon ($C_{Polymer}$) into carbon dioxide ($C_{CO_2}$) by analyzing the amount of $CO_2$ evolved during aerobic soil incubation.[62] The respirometric data were plotted as the percentage of mineralization over an incubation period (115 days, Fig. 5A). The α-cellulose (positive control) exhibited the highest degree of biodegradation, reaching 78.7 ± 8.2% in 115 days, consistent with previous studies conducted under similar ISO 17556 or ASTM D5988 conditions.[63–65] On the other hand, LDPE (negative control) displayed minimal mineralization (3.67 ± 3.3%), which may be attributed to organic impurities introduced during the extrusion process, as hypothesized in our earlier study.[66] Similar minor degradation of LDPE in soil (2.5%, 134 days) has also been reported.[67]

The LANC film exhibited a mineralization level of 48.0 ± 4.7%, which decreased to 34.4 ± 0.9% upon the addition of PVA at a 50 wt% loading (LANC50PVA50), indicating that PVA adversely affected the biodegradation process. Rather than toxicity toward microbial communities, morphological characteristics could be considered the primary reason.[68] The strong and complex inter-/intramolecular hydrogen bonding networks in LANC50PVA50 increased the film's stiffness (as reflected by Young's modulus, Table S5), which limited the accessibility for the penetration of microbial enzymes into the polymer matrix.[67] Furthermore, the hydrophobicity and low water vapor permeability of LANC50PVA50 also impeded its affinity for water and exposure to enzymes, making it less susceptible to hydrolysis and microbial degradation.[69] This observation aligns with previous findings, which reported reduced degradation of PVA/sugar cane bagasse (SCB) films (23.7%) compared to PVA-free SCB films (34.4%) in soil.[70] Similarly, other research revealed that PVA exhibits limited mineralization in soil due to the lack of specific degrading microorganisms and its tendency to adsorb onto organic and inorganic soil matter.[71] Despite this fact, the slow deterioration of PVA and lignocellulosic biomass may not negatively impact plant growth or crop production due to their inherently low toxicity and environmental friendliness.[72]

To better quantify and compare the biodegradation profiles, the mineralization curves were fitted with first-order kinetic and Hill-like models (Fig. 5A). The fitting parameters, the sum of residuals ($\chi^2$), and correlation coefficient ($R^2$) are summarized (Table S7). The Hill-like model more accurately described the biodegradation kinetics of all samples, likely due to the complex degradation behavior driven by diverse microbial communities in soil.[73,74] The biodegradation performance was also compared with other (commercial) mulch films' biodegradation rates, tested under similar ISO 17556 or ASTM 5988 conditions (Fig. 5B). The results indicate that the LANC50PVA50 mulch film is comparable to most available commercial films, highlighting its potential for practical applications. While EN 17033 specifies >90% disintegration/biodegradation within two years under controlled conditions, our mineralization data represent a more conservative estimate. Increasing soil moisture has been shown to substantially accelerate biodegradation in closed-system respirometry tests; for instance, Novamont reported a huge elevation in the speed of biodegradation of their commercial mulch film (Master-Bi HF03V), from 37% to 88% within 115 days by raising the water content of soil from 25% to 80% of its maximum water-holding capacity.[75] This suggests that further optimization of soil conditions may enhance the biodegradation rate of our films.

The changes in the morphological properties and molecular structure of the LANC50PVA50 mulch film, presumably caused by microbial activity during 60 days of soil burial (denoted as LANC50PVA50_D0 and LANC50PVA50_D60), were observed by SEM and evaluated by FT-IR measurements, respectively. The FTIR spectra of the soil-degraded

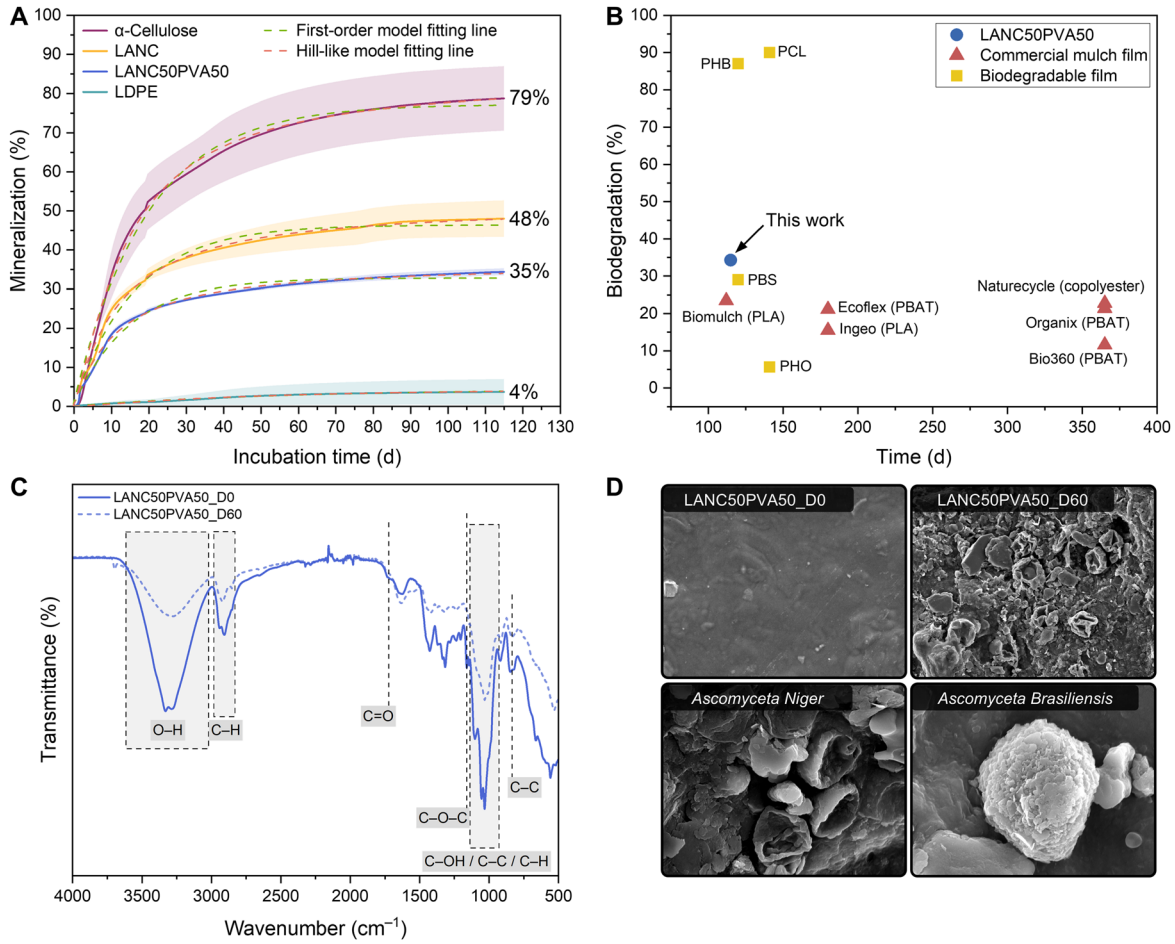


**Fig. 5** (A) Biodegradation curves and kinetic model fitted curve of LANC, LANC50PVA50, α-cellulose (positive reference) and LDPE (negative reference). Mean mineralization values (lines) were plotted with highlighted areas around curves that correspond to the standard deviation of triplicates for LANC and LANC50PVA50, and duplicates for references. (B) Comparison of mineralization for LANC50PVA50 with that for commercial mulch films and biodegradable plastics, conducted under ambient soil environment conditions (ISO 17556 or ASTM 5988). Detailed information on biodegradable plastics and commercial mulch films can be found in Table S8. (C) FTIR spectra of LANC50PVA50 film before and after soil burial biodegradation for 60 days. (D) Scanning electron microscopy (SEM) micrographs depicting the top surface of samples at day 0 (D0) and day 60 (D60), showing the attachment of various microorganisms on the film surface (bottom images).

LANC50PVA50 film (Fig. 5C) reveal a noticeable decrease in the intensity of the C–OH, C–C, C–H, C–O–C, and O–H stretching regions, suggesting that microorganisms might utilize cellulose as a primary carbon source. Additionally, the reduction in the O–H stretching vibration peak may be linked to the consumption of glycerol and/or PVA by soil microbes. It is imperative that the PVA backbone potentially underwent partial hydrolysis, as evidenced by minor decreases in the characteristic PVA peaks at 840 $cm^{-1}$ (C–C stretching) and 1450 $cm^{-1}$ (C–H bending). Moreover, SEM images revealed progressive surface erosion, including the formation of cavities, voids, and pits on the buried film (Fig. 5D), suggesting that biodegradation by microorganisms occurred readily under ambient soil conditions. Microbial colonization was also clearly visible. The spores of specific fungi possibly belonging to the phylum *Ascomycota* (*e.g.*, *A. Niger* and *A. Brasiliensis*),[76] known as polymer degraders in terrestrial environments,[62] were observed colonizing the film surface. Unique frustules and long filaments from other fungi, as well as unicellular organisms (*e.g.*, diatoms), were also present. Interestingly, regions colonized by microorganisms exhibited more pronounced surface erosion than uncolonized areas (Fig. S8), suggesting localized secretion of depolymerases to destroy the nearby polymer matrix, and facilitate substrate consumption.[77] However, further studies on these microbial communities using next-generation sequencing analysis could be performed to elucidate their eventual roles in the biodegradation mechanism.[66,78]

**3.2.6. Phytotoxicity tests using plant models.** The potential ecotoxicity of the LANC50PVA50 mulch film after its service life was evaluated (Fig. 6). Exposure to fragmented LANC50PVA50 and LDPE films (10 wt%) had no significant impact on the germination rate of either ryegrass (96.7 ± 5.77%) or tatsoi (100%). In contrast, the presence of $CdCl_2$-1% in the soil caused a minor reduction in germination rate for ryegrass (93.3%) and a complete inhibition for tatsoi (0%), highlighting

 

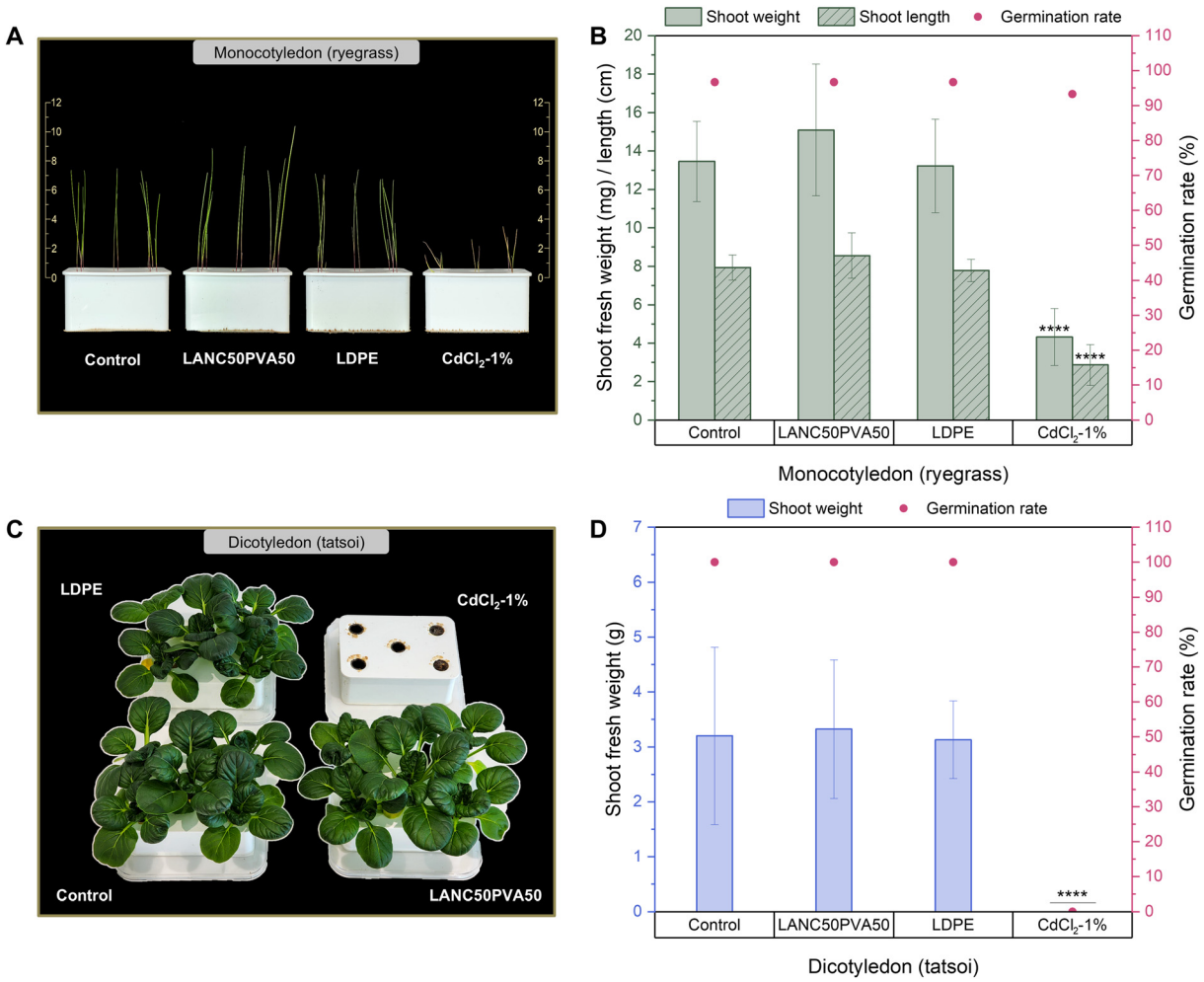


**Fig. 6** (A) and (C) Digital photographs of the monocotyledon (ryegrass) and dicotyledon (tatsoi) on day 14 and 55, respectively. Effect of LANC, LANC50PVA50, LDPE films and $CdCl_2$-1% (negative reference) on (B) germination rate, shoot fresh weight, and shoot length of ryegrass, and (D) germination rate, shoot fresh weight of tatsoi. Error bars are standard deviations of the mean ($n$ = 30 for ryegrass and $n$ = 5 for tatsoi). The asterisks on top of bars refer to the statistically significant difference compared to control samples (*$P$ < 0.05, **$P$ < 0.01, ***$P$ < 0.001, ****$P$ < 0.0001).

its phytotoxicity. Furthermore, the shoot fresh weight and height of ryegrass displayed no statistically significant differences between the buried LANC50PVA50 film and the film-free control ($P$ > 0.05), apart from $CdCl_2$-1% that drastically inhibited the ryegrass growth ($P$ < 0.0001). A similar trend was observed for tatsoi, with no significant differences between control and mulch film treatments, except in the $CdCl_2$-1% group. It is interesting to note that in the case of ryegrass, slightly higher shoot fresh weight and length were observed in the LANC50PVA50 treatment group compared to the control (15.1 ± 3.4 *versus* 13.5 ± 2.1 mg, and 8.56 ± 0.04 *versus* 7.94 ± 0.07 cm, respectively). This slight increase in ryegrass yield may result from improved soil moisture retention provided by the mulch material,[79] rather than from any nutrient contributions from the film. The tatsoi results showed no such effect, likely because its faster growth rate makes it less sensitive to small variations in soil moisture. These findings suggest that our proposed mulch film, after its service life, does not exert noticeable ecotoxic effects on seed germination or early plant growth of monocotyledonous (ryegrass) and dicotyledonous (tatsoi) species.

**3.2.7. Anti-drought performance of mulching films.** The water retention behavior of the LANC50PVA50 sample was observed to assess its practical application as a mulch film by monitoring the growth of ryegrass (Fig. 7). Ryegrass grown in vials covered with the film exhibited significantly better growth than in uncovered vials, with higher shoot fresh weight (17.7 ± 2.3 *versus* 10.9 ± 2.0 mg, $P$ < 0.0001) and greater shoot length (10.8 ± 0.9 *versus* 8.4 ± 0.6 cm, $P$ < 0.001). In addition, the remaining soil moisture content in film-covered vials showed a trivial decrease (11%) after 14 days, compared to much more substantial moisture loss (37%) in the uncovered vials. As water was the only differing variable in the experiment, the enhanced growth clearly indicates the film's ability to reduce evaporative losses. Moreover, vials covered with films without holes demonstrated excellent moisture retention, with

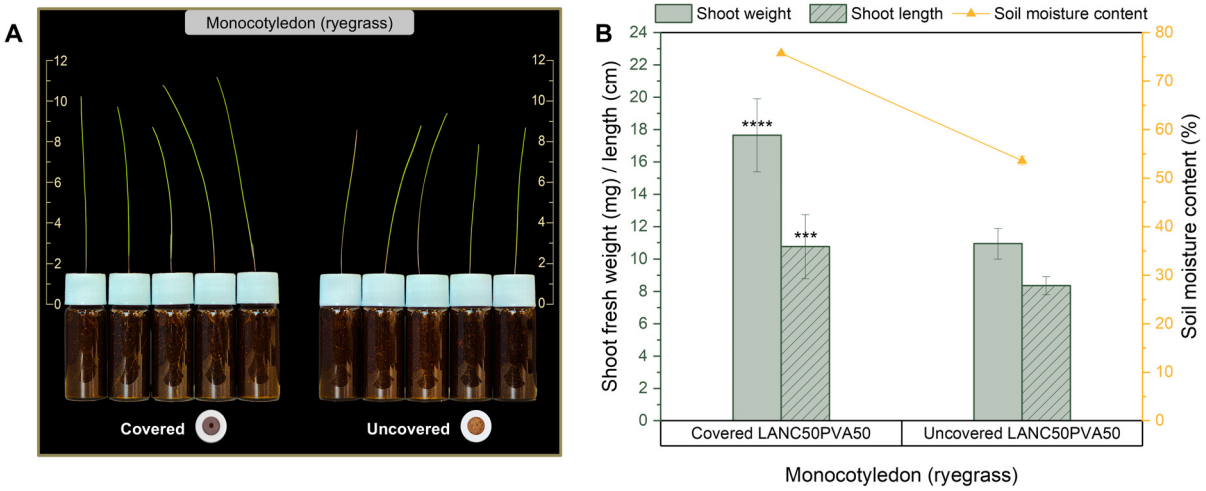


Fig. 7 (A) Digital photographs of ryegrass in LANC50PVA50 film-covered (left) and film-uncovered (right) soil vials on day 14. (B) Comparison of ryegrass growth (shoot wet weight and shoot length) and moisture retention capacity. The germination rates of ryegrass in this test are 100%. Error bars are standard deviations of the mean ($n$ = 15). The asterisks on top of bars refer to the statistically significant difference between film covered and uncovered samples (*$P$ < 0.05, **$P$ < 0.01, ***$P$ < 0.001, ****$P$ < 0.0001).

only 5% moisture loss over 14 days, further supporting the film's suitability for conserving soil moisture during seed germination and early plant establishment.

### 3.3. Sustainability implications, challenges, and future perspectives

Dead leaves represent an abundant, non-edible biomass stream that is routinely collected as a seasonal waste in many regions, yet it is typically treated as a low-value material and routed to disposal pathways such as incineration or landfilling. In this work, dead leaves are valorized into functional agricultural mulch films, demonstrating a higher-value use of an underutilized feedstock. Importantly, the resulting lignocellulosic nanofiber (LCNF) fraction retains native lignin, which contributes to UV shielding and increased hydrophobicity, thereby providing functionality beyond simple cellulose extraction and reducing the need for additional UV stabilizers or hydrophobizing additives. Where municipal or institutional leaf-collection infrastructure already exists, partnerships with local governments or institutions could potentially redirect a portion of this stream from disposal to upcycling into manufacturing feedstocks, which may reduce marginal feedstock procurement burdens and contribute to reduced waste management pressure. Notably, a preliminary robustness test using another dead-leaf species (*Zelkova serrata*) produced films with tensile strength, WCA and WVP values comparable to those from the primary leaf source (Fig. S10), suggesting that dead-leaf feedstocks are broadly compatible with this process and that leaf-to-leaf variability may not be a major limiting factor within the tested species. Nevertheless, mixed-species streams and seasonal or site-dependent differences may affect pretreatment efficiency and film performances; therefore, systematic evaluation of preprocessing strategies to convert heterogeneous leaf streams into a more consistent feedstock will be an important consideration during scale-up.

From a process perspective, our strategy integrates DES pretreatment with fully water-based film fabrication, thereby avoiding the use of strong acids, alkalis, or volatile organic solvents during film processing. This approach aligns with key green chemistry principles (renewable feedstocks, benign solvents in formulation, and design for degradation) and can reduce hazards associated with solvent handling and waste management burdens compared with conventional processing routes. Nevertheless, during pretreatment, solvent loss during separation and the accumulation of dissolved organics (*e.g.*, partially solubilized lignin/hemicellulose/extractives) in the recovered DES may reduce pretreatment efficiency upon reuse, potentially affecting fibrillation quality and downstream performance. Accordingly, improving recovery efficiency and maintaining DES compositional stability represent important directions for future optimization. Additionally, alternative DES formulations that enable lower solvent usage, higher solids loading, and improved recyclability should be explored in future work.

Scale-up of film production is another key consideration. While laboratory casting is effective for proof-of-concept demonstration and mechanistic evaluation, industrial mulch films are commonly manufactured using high-throughput processes such as extrusion, calendering/lamination, and roll-to-roll casting. These established platforms could be adapted to LANC/PVA systems, for example through continuous coating/casting of aqueous suspensions followed by controlled drying and post-processing (Fig. S11). However, further optimization will be required to reproduce laboratory-scale microstructural characteristics and field-relevant performance under continuous manufacturing conditions.

Finally, a screening cost estimate (Table S10) suggests that the estimated production cost of LANC50PVA50 film (0.38 USD

per $m^2$) falls within the range of several commercially available biodegradable mulch films, such as Bio360 (0.78–0.86 USD per $m^2$) and a cornstarch-based film (0.72 USD per $m^2$) (Table S11). Although it remains higher than non-biodegradable PE mulch film (0.29 USD per $m^2$) when considering purchase price alone, a fair comparison should consider whole-life cost, including both manufacturing and end-of-life burdens. In practical mulch film applications, PE film often requires post-season retrieval, transport, and disposal/recycling, and incomplete recovery or fragmentation can contribute to persistent residues and microplastic accumulation in agricultural soils. In contrast, biodegradable mulch systems are intended to reduce end-of-life collection burdens and long-term residue accumulation, which may translate into lower handling costs and environmental impacts depending on local practice and regulatory frameworks. Future work should therefore combine pilot-scale manufacturing trials with rigorous techno-economic and life-cycle assessments, alongside longer-term field validation, to quantify tradeoffs and identify the most impactful levers for sustainable deployment.

## 4. Conclusions

This study demonstrated the upcycling of waste lignocellulosic biomass (dead leaves) into lignin-containing nanocellulose fibrils (LCNFs) through a green, solvent-based pretreatment combined with ultrasonication. These LCNFs were blended with cellulose nanocrystals (CNCs), polyvinyl alcohol (PVA), and glycerol (Gly) using an aqueous solution to fabricate biodegradable films *via* evaporation-induced self-assembly. The resulting LANC/PVA composite films exhibited outstanding functional properties due to the synergistic hydrogen bonding among their constituents. These included high tensile strength (TS = 20–24 MPa), complete UV shielding (~100% for UVA and UVB), notable hydrophobicity (WCA = 77.8–118.6°) and strong moisture vapor barrier performance (WVP = 1.93–5.7 g μm ($m^2$ day Pa)$^{-1}$). These characteristics fulfill the key performance criteria required for agricultural mulch films, such as minimizing water loss and inhibiting weed growth, which were corroborated through controlled germination and moisture retention experiments.

Furthermore, the films demonstrated a biodegradation profile comparable to that of commercial biodegradable mulch films under ambient soil conditions. Importantly, no measurable phytotoxicity was observed after their service life, indicating environmental compatibility and safety for plant germination and development. Our approach contributes to the development of sustainable materials by transforming readily available biomass waste into high-performance biodegradable plastics, thereby aligning with circular economy principles and promoting responsible plastic use in horticulture and agriculture. Future research will focus on elucidating the roles of soil microbial consortia in film degradation and conducting field-scale trials to assess long-term impacts on crop productivity and soil quality.

## Author contributions

Pham Thanh Trung Ninh: conceptualization, methodology, investigation, data curation, writing – original draft, writing – review & editing, visualization. Shinhyeong Choe: investigation, data curation, writing – original draft, writing – review & editing, visualization. Yongjun Cho: investigation, data curation, writing – original draft, writing – review & editing. Hoseong Moon: investigation, writing – review & editing. Jaewook Myung: conceptualization, writing – original draft, writing – review & editing, supervision, project administration, funding acquisition.

## Conflicts of interest

There are no conflicts to declare.

## Data availability

The data supporting this article have been included as part of the supplementary information (SI). Supplementary information is available. See DOI: https://doi.org/10.1039/d5gc06616f.

Further relevant datasets are accessible from the corresponding author upon reasonable request.

## Acknowledgements

This research was supported by the National Research Foundation of Korea (NRF) grant funded by the Korea government (MSIT) (RS-2023-00209472), by the Ministry of Oceans and Fisheries, Korea (20200104), and by the grant for the "KAIST Grand Challenge 30 Program" funded by the Korea Advanced Institute of Science and Technology (N11250072). This work was also supported by the National Institute for International Education (NIIED) and the Hyundai Motor Chung Mong-Koo Foundation.

## References

1 Y. Yu and M. Flury, *npj Mater. Sustain.*, 2024, **2**, 9.
2 M. Bergmann, F. Collard, J. Fabres, G. W. Gabrielsen, J. F. Provencher, C. M. Rochman, E. van Sebille and M. B. Tekman, *Nat. Rev. Earth Environ.*, 2022, **3**, 323–337.
3 J. W. Cottom, E. Cook and C. A. Velis, *Nature*, 2024, **633**, 101–108.
4 A. S. Pottinger, R. Geyer, N. Biyani, C. C. Martinez, N. Nathan, M. R. Morse, C. Liu, S. Hu, M. de Bruyn, C. Boettiger, E. Baker and D. J. McCauley, *Science*, 2024, **386**, 1168–1173.
5 OECD, *Global Plastics Outlook: Policy Scenarios to 2060*, OECD Publishing, 2022, https://www.oecd.org/en/publi-

cations/global-plastics-outlook_aa1edf33-en.html, (accessed September 2025).
6 T. Hofmann, S. Ghoshal, N. Tufenkji, J. F. Adamowski, S. Bayen, Q. Chen, P. Demokritou, M. Flury, T. Hüffer, N. P. Ivleva, R. Ji, R. L. Leask, M. Maric, D. M. Mitrano, M. Sander, S. Pahl, M. C. Rillig, T. R. Walker, J. C. White and K. J. Wilkinson, *Commun. Earth Environ.*, 2023, **4**, 332.
7 C. Campanale, S. Galafassi, F. Di Pippo, I. Pojar, C. Massarelli and V. F. Uricchio, *TrAC, Trends Anal. Chem.*, 2024, **170**, 117391.
8 J. D. Estrada-Sotomayor, Ł. Łopusiewicz, E. Lizundia, S. Guenther and D. Merino, *Green Chem.*, 2025, **27**, 4587–4602.
9 H. Simon, F. Emma, M. Star, S. Chris, E. Laurence, K. Maryann, K. Alima, S. Sergio and M. Veronica, *Relevance of Conventional and Biodegradable Plastics in Agriculture*, European Commission DG Environment, 2021, https://environment.ec.europa.eu/system/files/2021-09/Agricultural%20Plastics%20Final%20Report.pdf, (accessed October 2025).
10 L. Xiong, Z. Li, F. Shah, P. Wang, Q. Yuan and W. Wu, *Chem. Eng. J.*, 2024, **492**, 152219.
11 European Bioplastic, *Alternative feedstock for biobased plastics: Bridging the gap between research and the market (White Paper)*, Zenodo, 2024, https://zenodo.org/records/14245778, (accessed April 2025).
12 European Bioplastic, *Continuous growth - global production capacities of bioplastics 2024–2029*, 2024, https://www.european-bioplastics.org/bioplastics-market-development-update-2024/, (accessed April 2025).
13 T. Narancic, S. Verstichel, S. R. Chaganti, L. Morales-Gamez, S. T. Kenny, B. D. Wilde, R. B. Padamati and K. E. O'Connor, *Environ. Sci. Technol.*, 2018, **52**, 10441–10452.
14 J.-G. Rosenboom, R. Langer and G. Traverso, *Nat. Rev. Mater.*, 2022, **7**, 117–137.
15 A. K. Mohanty, S. Vivekanandhan, J.-M. Pin and M. Misra, *Science*, 2018, **362**, 536–542.
16 A. D. J. Vargas-Soplín, A. Prochnow, C. Herrmann, B. Tscheuschner and U. Kreidenweis, *Resour., Conserv. Recycl.*, 2022, **187**, 106598.
17 S. Fang, X. Lyu, T. Tong, A. I. Lim, T. Li, J. Bao and Y. H. Hu, *Nat. Commun.*, 2023, **14**, 1203.
18 F. Bello and M. S. Peresin, *Food Hydrocolloids*, 2024, **157**, 110378.
19 M. Fazeli, S. Mukherjee, H. Baniasadi, R. Abidnejad, M. Mujtaba, J. Lipponen, J. Seppälä and O. J. Rojas, *Green Chem.*, 2024, **26**, 593–630.
20 E. Rojo, M. S. Peresin, W. W. Sampson, I. C. Hoeger, J. Vartiainen, J. Laine and O. J. Rojas, *Green Chem.*, 2015, **17**, 1853–1866.
21 A. Najahi, Q. Tarrés, M. Delgado-Aguilar, J. L. Putaux and S. Boufi, *Biomacromolecules*, 2023, **24**, 3872–3886.
22 C. Scopetani, J. Pellinen and S. Selonen, *Environ. Res.*, 2024, **255**, 119177.
23 I. Leppänen, A. Hokkanen, M. Österberg, M. Vähä-Nissi, A. Harlin and H. Orelma, *Cellulose*, 2022, **29**, 8551–8567.
24 N. Nasiri, H. E. Cainglet, J. R. Black, G. Garnier and W. Batchelor, *Biomacromolecules*, 2025, **26**, 248–257.
25 J.-K. Kim, S. H. Oh, M.-O. Song, S. Jang, S. J. Kang, S. K. Kwak and J. Jin, *Composites, Part B*, 2024, **281**, 111563.
26 A. Avella, M. R. T. Leggieri, A. E. Alexakis, E. Malmström and G. L. Re, *ACS Appl. Mater. Interfaces*, 2025, **17**, 2602–2614.
27 X. Wang, M. Li, Y. Xiong, H. Qin, Q. Li, F. Zhang, Y.-L. Yu and G. Qing, *Small*, 2025, **21**, 2408695.
28 W. Liu, A. Shomali, C. Zhang, B. Coasne, J. Carmeliet and D. Derome, *Carbohydr. Polym.*, 2024, **343**, 122429.
29 T. Begum, P. A. Follett, L. Jaiswal, D. de Guibert, S. Salmieri and M. Lacroix, *Food Hydrocolloids*, 2024, **150**, 109697.
30 S. Wang, Z. Yu, X. Sun, M. Panahi-Sarmad, P. Yang, P. Zhu, Y. Zhu, H. Liu and F. Jiang, *Adv. Mater.*, 2025, **37**, 2416916.
31 J. Zeng, Y. Ma, P. Li, X. Zhang, W. Gao, B. Wang, J. Xu and K. Chen, *Carbohydr. Polym.*, 2024, **330**, 121824.
32 K. S. Salem, N. K. Kasera, M. A. Rahman, H. Jameel, Y. Habibi, S. J. Eichhorn, A. D. French, L. Pal and L. A. Lucia, *Chem. Soc. Rev.*, 2023, **52**, 6417–6446.
33 D. Merino, A. Zych and A. Athanassiou, *ACS Appl. Mater. Interfaces*, 2022, **14**, 46920–46931.
34 Y. Wang, J. Su, T. Li, P. Ma, H. Bai, Y. Xie, M. Chen and W. Dong, *ACS Appl. Mater. Interfaces*, 2017, **9**, 36281–36289.
35 A. Harvey, *Thermodynamic Properties of Water: Tabulation From the IAPWS Formulation 1995 for the Thermodynamic Properties of Ordinary Water Substance for General and Scientific Use*, 1998, DOI: 10.6028/NIST.IR.5078.
36 X. Shi, Z. Wang, S. Liu, Q. Xia, Y. Liu, W. Chen, H. Yu and K. Zhang, *Nat. Sustain.*, 2024, **7**, 315–325.
37 I. Petit, G. D. Belletti, T. Debroise, M. J. Llansola-Portoles, I. T. Lucas, C. Leroy, C. Bonhomme, L. Bonhomme-Coury, D. Bazin, M. Daudon, E. Letavernier, J. P. Haymann, V. Frochot, F. Babonneau, P. Quaino and F. Tielens, *ChemistrySelect*, 2018, **3**, 8801–8812.
38 Z. Yi, S. Fu, Y. Wang, J. Ai, C. Hu, S.-Y. Leu and A. Halim, *ACS Sustainable Chem. Eng.*, 2024, **12**, 7802–7812.
39 Y. Ding, M. Liu, F. Zhang, B. Zhong, T. Yang, X. Ding, C. Liu, P. Zhang and Z. Chi, *ACS Sustainable Chem. Eng.*, 2024, **12**, 7443–7456.
40 S. A. Khan, M. A. Ahmed, M. M. Baig, M. M. Rehman, Y. Yang, S. G. Lee, J. W. Choi and W. Y. Kim, *Chem. Eng. J.*, 2024, **485**, 149660.
41 N. Wahlström, U. Edlund, H. Pavia, G. Toth, A. Jaworski, A. J. Pell, F. X. Choong, H. Shirani, K. P. R. Nilsson and A. Richter-Dahlfors, *Cellulose*, 2020, **27**, 3707–3725.
42 Q. Xia, C. Chen, Y. Yao, J. Li, S. He, Y. Zhou, T. Li, X. Pan, Y. Yao and L. Hu, *Nat. Sustain.*, 2021, **4**, 627–635.
43 M. Parit, H. Du, X. Zhang and Z. Jiang, *ACS Appl. Polym. Mater.*, 2022, **4**, 3587–3597.
44 J. V. Vermaas, M. F. Crowley and G. T. Beckham, *ACS Sustainable Chem. Eng.*, 2019, **7**, 19570–19583.
45 A. Etale, A. J. Onyianta, S. R. Turner and S. J. Eichhorn, *Chem. Rev.*, 2023, **123**, 2016–2048.
46 H. L. Ornaghi, F. G. Ornaghi, R. M. Neves, F. Monticeli and O. Bianchi, *Cellulose*, 2020, **27**, 4949–4961.

 

47 H. Li, A. Kulachenko, A. P. Mathew, R. B. Stoltz and O. Sevastyanova, *ACS Sustainable Chem. Eng.*, 2023, **11**, 16793–16805.
48 M. Nuruddin, D. M. Korani, H. Jo, R. A. Chowdhury, F. J. Montes, J. A. Howarter and J. P. Youngblood, *ACS Appl. Polym. Mater.*, 2020, **2**, 4405–4414.
49 E. Missale, D. Maniglio, G. Speranza, M. Frasconi and M. F. Pantano, *ACS Appl. Nano Mater.*, 2024, **7**, 18167–18176.
50 A. Halloub, M. Raji, H. Essabir, H. Chakchak, R. Boussen, M.-O. Bensalah, R. Bouhfid and A. E. K. Qaiss, *Carbohydr. Polym.*, 2022, **296**, 119972.
51 Y. Li, S. Zhao, D. Hu, A. J. Ragauskas, D. Cao, W. Liu, C. Si, T. Xu, P. Zhao, X. Song and K. Li, *ACS Sustainable Chem. Eng.*, 2022, **10**, 11856–11866.
52 F. Seidi, Y. Liu, Y. Huang, H. Xiao and D. Crespy, *Chem. Soc. Rev.*, 2025, **54**, 3140–3232.
53 A. Hambardzumyan, L. Foulon, B. Chabbert and V. Aguié-Béghin, *Biomacromolecules*, 2012, **13**, 4081–4088.
54 S. Rodríguez-Fabià, J. Torstensen, L. Johansson and K. Syverud, *Cellulose*, 2022, **29**, 5375–5393.
55 E. Ruggeri, D. Kim, Y. Cao, S. Farè, L. De Nardo and B. Marelli, *ACS Sustainable Chem. Eng.*, 2020, **8**, 14312–14321.
56 T. D. Bui, Y. Wong, K. Thu, S. J. Oh, M. K. Ja, K. C. Ng, I. Raisul and K. J. Chua, *J. Appl. Polym. Sci.*, 2017, **134**, 44765.
57 S. J. Metz, W. J. C. van de Ven, J. Potreck, M. H. V. Mulder and M. Wessling, *J. Membr. Sci.*, 2005, **251**, 29–41.
58 F. Müller-Plathe, *J. Membr. Sci.*, 1998, **141**, 147–154.
59 H. Aloui, K. Khwaldia, M. Hamdi, E. Fortunati, J. M. Kenny, G. G. Buonocore and M. Lavorgna, *ACS Sustainable Chem. Eng.*, 2016, **4**, 794–800.
60 A. A. Benhamou, S. Boukind, H. Khalili, A. Moubarik, M. E. Achaby, Z. Kassab and H. Sehaqui, *ACS Appl. Polym. Mater.*, 2024, **6**, 2763–2776.
61 M. Basak, K. M. Y. Arafat, L. A. Lucia and L. Pal, *ACS Sustainable Chem. Eng.*, 2024, **12**, 15502–15514.
62 M. Sander, *Environ. Sci. Technol.*, 2019, **53**, 2304–2315.
63 M. Tosin, A. Pischedda and F. Degli-Innocenti, *Polym. Degrad. Stab.*, 2019, **166**, 213–218.
64 D. Briassoulis, A. Mistriotis, N. Mortier and M. Tosin, *J. Cleaner Prod.*, 2020, **242**, 118392.
65 J. Šerá, L. Serbruyns, B. De Wilde and M. Koutný, *Polym. Degrad. Stab.*, 2020, **171**, 109031.
66 A. Camus, S. Choe, C. Bour-Cardinal, J. Isasmendi, Y. Cho, Y. Kim, C. V. Irimia, C. Yumusak, M. Irimia-Vladu, D. Rho, J. Myung and C. Santato, *Commun. Mater.*, 2024, **5**, 173.
67 P. Pfohl, D. Bahl, M. Rückel, M. Wagner, L. Meyer, P. Bolduan, G. Battagliarin, T. Hüffer, M. Zumstein, T. Hofmann and W. Wohlleben, *Environ. Sci. Technol.*, 2022, **56**, 16873–16884.
68 G. Tian, L. Li, Y. Li and Q. Wang, *ACS Omega*, 2022, **7**, 42515–42523.
69 M. Ghasemlou, F. Daver, B. J. Murdoch, A. S. Ball, E. P. Ivanova and B. Adhikari, *Sci. Total Environ.*, 2022, **815**, 152684.
70 A. Corti, P. Cinelli, S. D'Antone, E.-R. Kenawy and R. Solaro, *Macromol. Chem. Phys.*, 2002, **203**, 1526–1531.
71 E. Chiellini, P. Cinelli, V. I. Ilieva and M. Martera, *Biomacromolecules*, 2008, **9**, 1007–1013.
72 J. D. Judy, M. Williams, A. Gregg, D. Oliver, A. Kumar, R. Kookana and J. K. Kirby, *Environ. Pollut.*, 2019, **252**, 522–531.
73 S. A. da Silva, D. J. L. Faccin and N. S. M. Cardozo, *ACS Sustainable Chem. Eng.*, 2024, **12**, 11856–11865.
74 M. V. Arcos-Hernandez, B. Laycock, S. Pratt, B. C. Donose, M. A. L. Nikolić, P. Luckman, A. Werker and P. A. Lant, *Polym. Degrad. Stab.*, 2012, **97**, 2301–2312.
75 S. Chinaglia, E. Esposito, M. Tosin, M. Pecchiari and F. D. Innocenti, *Polym. Degrad. Stab.*, 2024, **222**, 110691.
76 D. I. Haga, S. M. Burrows, R. Iannone, M. J. Wheeler, R. H. Mason, J. Chen, E. A. Polishchuk, U. Pöschl and A. K. Bertram, *Atmos. Chem. Phys.*, 2014, **14**, 8611–8630.
77 M. T. Zumstein, A. Schintlmeister, T. F. Nelson, R. Baumgartner, D. Woebken, M. Wagner, H.-P. E. Kohler, K. McNeill and M. Sander, *Sci. Adv.*, 2018, **4**, eaas9024.
78 M. Julinová, D. Šašinková, A. Minařík, M. Kaszonyiová, A. Kalendová, M. Kadlečková, A. Fayyazbakhsh and M. Koutný, *Biomacromolecules*, 2023, **24**, 4939–4957.
79 L. A. Lodi, R. Borges, R. Bortoletto-Santos, C. A. D. Oliveira-Paiva, C. Ribeiro and C. S. Farinas, *J. Environ. Chem. Eng.*, 2024, **12**, 114539.